Comparison of the extent and mass of CME events in the interplanetary medium using IPS and SMEI Thomson scattering observations

B. V. Jackson[a]; P. P. Hick[a]; A. Buffington[a]; M. M. Bisi[a]; M. Kojima[b]; M. Tokumaru[b]

[a] Center for Astrophysics and Space Sciences, University of California, San Diego, La Jolla, CA, USA [b] Solar-Terrestrial Environment Laboratory, Nagoya University, Aichi, Japan

PLEASE SCROLL DOWN FOR ARTICLE

Taylor & Francis
Taylor & Francis Group

Comparison of the extent and mass of CME events in the interplanetary medium using IPS and SMEI Thomson scattering observations

B. V. JACKSON*†, P. P. HICK†, A. BUFFINGTON†, M. M. BISI†, M. KOJIMA‡, and M. TOKUMARU‡

†Center for Astrophysics and Space Sciences, University of California, San Diego, 9500 Gilman Drive #0424, La Jolla, CA 92093-0424, USA
‡Solar-Terrestrial Environment Laboratory, Nagoya University, Furo-cho Chikusa-ku, Nagoya, Aichi, 464-8601, Japan

The Solar-Terrestrial Environment Laboratory (STELab), Japan, interplanetary scintillation (IPS) *g*-level and velocity measurements can be used to give the extent of CME disturbances in the interplanetary medium arising from the scattering of the radio waves from distant point-like natural sources through the intervening medium. In addition, white-light Thomson-scattering observations from the Solar Mass Ejection Imager (SMEI) have recorded the inner heliospheric response to several hundred CMEs. The work described here compares and details the difference in three-dimensional (3D) reconstructions for these two data sets for the well-observed 28 October 2003 halo CME seen in LASCO; this passed Earth on 29 October in the SMEI data at the same elongations as IPS *g*-level observations. The SMEI data analysis employs a 3D tomographic reconstruction technique that obtains perspective views from outward-flowing solar wind as observed from Earth, iteratively fitting a kinematic solar wind density model, and when available, including IPS velocity data. This technique improves the separation of the heliospheric response in SMEI from other sources of background noise, and also provides the 3D structure of the CME and its mass. The analysis shows and tracks outward the northward portion of a loop structure of this halo CME. We determine an excess mass for this structure of 6.7×10^{16} g and a total mass of 8.3×10^{16} g in the SMEI analysis, and these are comparable to values obtained using IPS *g*-level data and a 3D reconstruction technique developed for these data and applied to this event. We also extend further the application for these analyses.

Keywords: Thomson scattering; Interplanetary scintillation; Computer assisted tomography; Solar wind

1. Introduction

The corona and inner heliosphere experience strong perturbations from flares and mass-ejection transients. When directed toward Earth, these may cause dramatic and sometimes hazardous conditions in the Earth's environment. We use remote-sensing

---

*Corresponding author. Email: bvjackson@ucsd.edu

observations to study the physics and global properties of heliospheric structures. We determine the 3D total mass and energy content of transient CME structures and compare these results both with *in situ* spacecraft data and ground-based data. The present studies are primarily based on data from interplanetary scintillation (IPS) observations [1, 2] from the Solar Terrestrial Environment Laboratory (STELab), Nagoya University in Japan [3], and from Thomson-scattering white-light observations using the Solar Mass Ejection Imager (SMEI) [4], and to a lesser extent, observations from space-borne coronagraphs.

Determination of the global properties of a CME, its morphology, and its motion, requires that most of the CME be observed throughout the time during its outward motion from the Sun. We have developed a tomographic technique for heliospheric remote-sensing data obtained from a single observing location that reconstructs the density and velocity distributions of CMEs. This enables studying CMEs as they propagate through the inner heliosphere to the Earth. We apply this technique to data from both STELab IPS and SMEI.

Section 2 gives a brief description of the tomographic technique used with these remote sensing observations. In section 3, this technique is used to interpret data from the 28 October 2003 "Halloween storm" CME, and we show superimposed magnetic flux cylinder reconstructions from the Advanced Composition Explorer (ACE) spacecraft *in situ* data. Section 4 discusses the results of these analyses. Section 5 discusses the current possibility to determine magnetic fields remotely in the heliosphere using Faraday Rotation (FR) observations. We conclude in section 6.

2.   The UCSD tomographic 3D reconstruction technique

The University of California at San Diego (UCSD) analyses reconstructed co-rotating or time-varying solar wind velocity and density structures by applying an inversion technique to the IPS and SMEI data. On the assumption that structures change little except for co-rotation within one solar rotation, rotation alone yields sufficient information for reconstruction of the quiet corona. For this case, we employ a co-rotational model, which assumes that structures to the east and to the west of the Sun are the same, but viewed from a different perspective [5]. However, we also use a time-dependent 3D tomographic model. When a transient structure, such as a heliospheric response to a CME, is observed across a large range of solar elongations, it is in effect viewed from widely different directions. This changing perspective is exploited to reconstruct a 3D time-dependent solar wind model.

Both the co-rotating and time-dependent analyses incorporate the fact that line-of-sight observations are dominated by contributions from material closest to the Sun. However, no explicit assumptions are made about the distribution of velocity and density along these lines of sight. The inversion process begins with an assumed set of initial boundary conditions for the solar wind model at 15 solar radii. In the case of the time-dependent model and the low-resolution SMEI analyses so far, these boundaries are set at a regular time cadence (usually at half-day intervals centred at 00 UT and 12 UT). In the initial stage, these lower boundaries (source surfaces) are populated with an unstructured approximation of mass and velocity at that distance from the Sun. Currently, the model propagates mass and velocity outward from this source surface to beyond Earth using a purely kinematic model. The IPS observations are remotely sensed from as close to the Sun as 11.5° elongation and outward (the weak scattering regime at 327 MHz at which STELab operates). Each line of sight is carried to as distant as 2 AU from Earth. The highest signal weight from the observations generally comes from material at the point of closest approach to the line of sight to the Sun, with that point being near the Sun in the solar direction and close to Earth beyond about 60° elongation. At the ends of the lines of sight 2 AU from the Earth, signals from solar wind observations are

less than 5% of the average total values. The 3D model extends to 3 AU from the Sun, assumes purely radial outflow, and enforces conservation of mass and mass flux [4, 6]. Given the initial velocities and densities on the inner boundaries, a 3D kinematic solar wind model over time is propagated throughout the inner heliosphere.

Line-of-sight IPS scintillation (g-) levels and velocities are generated from the solar wind reconstructions that correspond to the appropriate weighting function for the frequency of the IPS data used, and for the SMEI Thomson scattering data. The differences between observed and modelled quantities are projected back onto the source surface, by tracing each solar wind packet within the 3D model back to its origin on the source surface. These differences are used to update the initial mass and velocity distributions on the source surface boundaries in the case of the time-dependent reconstruction. The tomographic inversion takes place on the inner boundary by iteratively fitting the model to the observations until a least-squares minimum of observations to the model is obtained. When the model does not reproduce the solar wind at large solar distances accurately enough, source-surface values are altered to improve the fit. Convergence is assumed when differences no longer change by more than a few percent. This usually occurs well within the maximum allowed 18 iterations.

Only a few tens of thousand lines of sight from SMEI, and only about one thousand lines of sight from the STELab IPS exist in any one given solar rotation. The spatial and temporal resolution is maintained by a set of Gaussian filters having a $1/e$ $5° \times 5°$ latitude and longitude resolution with a 0.35-day temporal cadence for the density structure of the time-dependent SMEI model, and a $1/e$ $15° \times 15°$ latitude and longitude resolution with a 0.75-day temporal cadence for the velocity structure of the time-dependent IPS model. This resolution is good enough to determine the large-scale structure of solar wind velocity and density. Tests show that a few iterations erase any specific residue of the initial boundary conditions. The technique has been used successfully to analyse solar wind co-rotating structures [5] and CME-associated velocity and density structures using both IPS and Thomson-scattering observations [6–8], and these compare favourably with other techniques used to invert the IPS data [9, 10].

3.   The 28 October 2003 CME

Although this CME has been analysed before [7], we present here previously unpublished results. Figure 1 shows two images of the 28 October 2003 CME obtained using the LASCO C2 and C3 coronagraphs [11], and two 3D reconstructed images, one using SMEI with STELab IPS velocities, and the other using IPS g-levels and velocities.

The halo CME shows a far greater bright structure to the south of the Sun than to the north in the coronagraph images, while the opposite is true in the SMEI reconstructed images. The IPS reconstructed g-level map (figure 1d) shows this CME structure to the solar northeast, and another high g-level structure to the west. Figure 2 shows four 3D reconstructions of the 28 October 2003 CME. Figure 2a shows the density reconstruction using SMEI Thomson-scattering observations combined with IPS velocity analyses from [7]. Figures 2b and 2d show this same time period reconstructed from the STELab IPS g-level data using two different 3D reconstruction techniques. In figure 2b, the technique developed by [9, 10] determines if the CME is loop-shaped and the IPS data centred at the time indicated is fitted iteratively to this shape. There are very few IPS sources to the south during this period of STELab observations, and in the structure there is an extrapolation from observed sources to the north on this day. In figure 2d, the UCSD technique employs IPS g-level data and IPS velocity data to reconstruct the structure at the time given; since there is little IPS information available to the south at this time, no structure to the south appears in this image, or for that matter, in figure 1d.
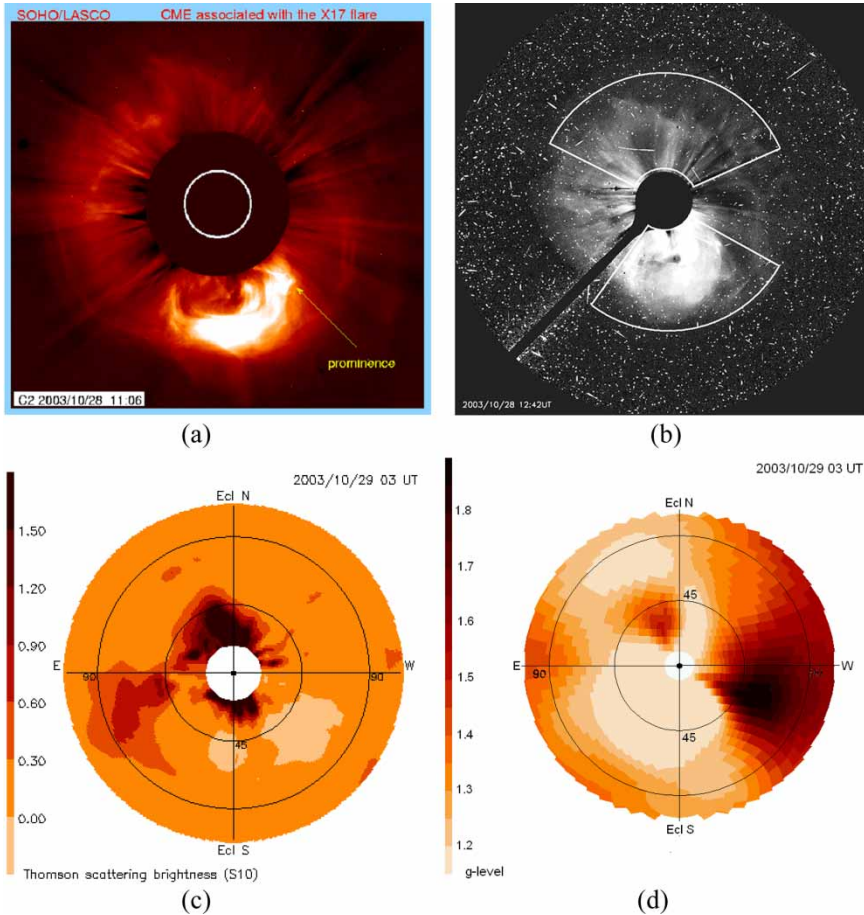
Figure 1. (a) A LASCO C2 coronagraph image of the 28 October 2003 CME at 11:06 UT. The most prominent structure is the bright material to the south of the Sun that is associated partially with prominence material. The outer edge of the field of view is at 6 Rs. (b) LASCO C3 coronagraph images obtained at 12:42 UT 28 October 2003. The outer edge of the field of view is 30 Rs. The regions to the south and north indicate locations used to determine columnar densities from the CME brightness by subtraction of a prior image not containing the CME (images and analysis courtesy of A. Vourlidas, private communication, 2005). (c) SMEI 3D reconstructed brightness image interpolated from Thomson-scattering derived volumes. An r^{-2} density fall-off has been removed from the volumes to show structure continuity from close to the Sun to distant from it. The Sun is centred with circles at 45° and 90° elongation indicated. (d) IPS g-level 3D reconstructed image interpolated from low-resolution g-level derived volumes at 03:00 UT on 29 October 2003 (the same time as in c). We attribute a high g-level feature to the west as due potentially either to noise or to signal from the ionospheric shock response at Earth.

The structures to the north have about the same radial distance in figures 2a and 2b. Figure 2c gives an overall view of the CME heliospheric dense structure as it has expanded outward between the orbit of Earth and the orbit of Mars. Here, the CME structure of the dense region observed in the heliosphere appears more loop-like. In figure 2d, the structure is highlighted above the $10\,e^-\,cm^{-3}$ level to show the location defining the 3D structure and above which the excess mass for the event is determined. To provide the calibration for this event, the same conversion factors used for the Bastille-day CME (14 July 2000) were used to reconstruct this CME [6, 12]. To determine excess CME mass, the region above a certain level is approximated by cubes, and the mass within the total of these cubes is summed. The defined region also defines an ambient solar wind mass which in this instance is assumed to be $5\,e^-\,cm^{-3}$ at 1 AU, and is scaled to higher values (using an r^{-2} density fall-off) at nearer distances to the Sun [7].
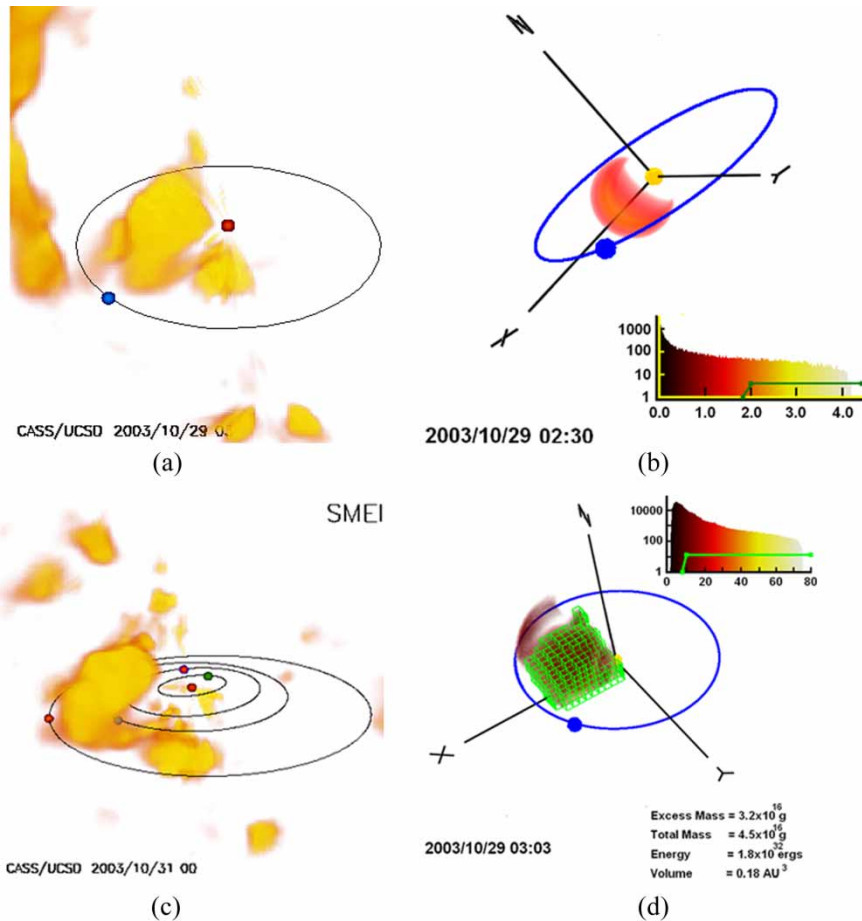
Figure 2. (a) 3D density reconstruction from Thomson-scattering SMEI observations of the heliospheric response to the 28 October 2003 CME viewed from 3 AU 30° above the ecliptic plane and 45° West of the Sun–Earth line. The Earth is indicated as a blue circle in its elliptical orbit; the Sun by a red circle at the centre. Contours are from $10\,e^-\,cm^{-3}$ to $30\,e^-\,cm^{-3}$ and have an r^{-2} density gradient removed (from [7]). (b) STELab 3D reconstruction in g-level of the 28 October 2003 CME (from [10]). The Earth is again depicted on its orbit in blue. A histogram gives the range of g-levels depicted in the reconstruction. (c) UCSD SMEI 3D density reconstruction of the 28 October CME at a slightly later time showing its extent as the main portion of the density in the ecliptic traverses between Earth and Mars. The orbits of all the inner planets are shown for scale. (d) UCSD 3D IPS reconstruction of the same event from g-level data. As in the SMEI analysis in (a), contours are shown upward from $10\,e^-\,cm^{-3}$ and have an r^{-2} density gradient removed from the density analysis. The dense structure to the solar West shown in figure 1d is not shown in this reconstruction.

Similar to figure 2d, the masses of the CME and its energy can be determined by approximating the CME using cubes, and these mapped from one 3D reconstructed volume to the other. Figure 3 demonstrates how this is accomplished. Because a CME volume is not *a priori* defined, the data itself must be used to do this. One technique developed at UCSD allows the CME extent to be mapped in one reconstructed dataset by measuring all material present above a certain defined contour, and then summing the material within this volume to determine both the 3D structure and the value of the material contained within the volume. In the case of density, the material above a certain "ambient" density can be highlighted, approximated by cubes, and the mass of the material within each cube summed after removing the r^{-2} factor in order to provide a total sum of the material within the volume. The contour limit also defines the CME volume within this boundary and this can then be used to determine the
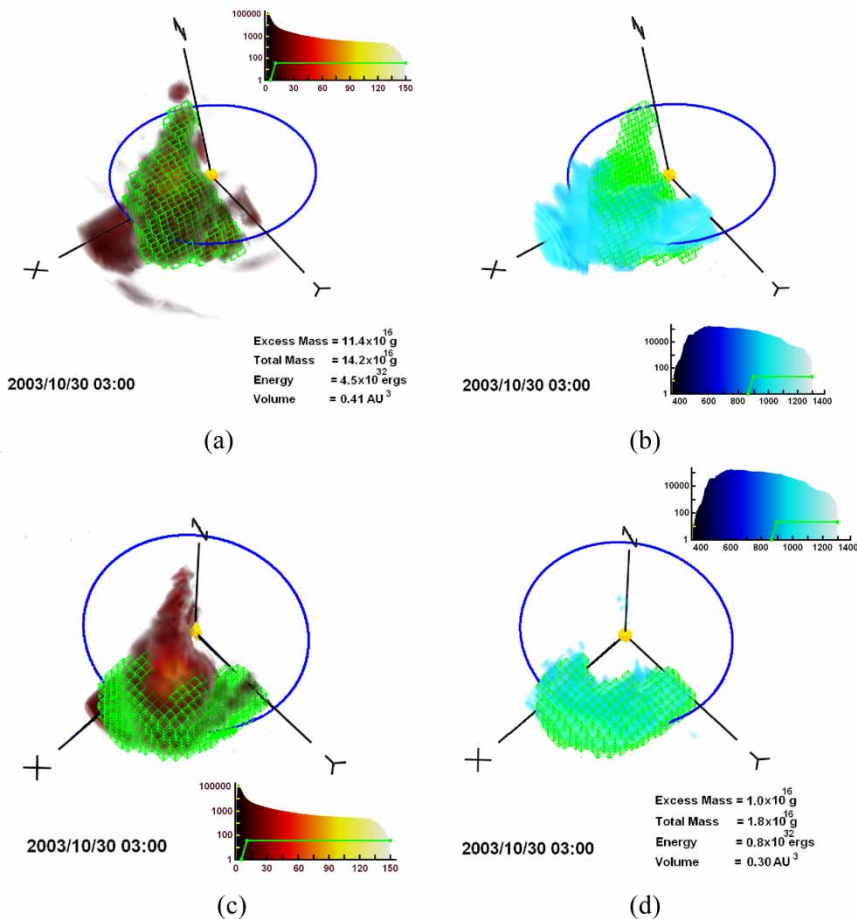
Figure 3.   3D reconstruction of the heliospheric response to the 28 October 2003 CME using SMEI Thompson-scattering and IPS velocity data similar to figure 2a at 00 UT on 30 October 2003. (a) The SMEI CME density structure above $10\,e^-\,cm^{-3}$ is highlighted by cubes, and this structure is transferred to (b) the 3D IPS velocity reconstruction to map cube by cube to the velocities associated with the dense structure. (c) The 3D SMEI density reconstruction in this volume has had from (d) the CME velocity structure above $900\,km\,s^{-1}$ highlighted by cubes displayed in this volume transferred to it to map cube by cube to the densities associated with the high velocity structure.

ambient mass within the volume. This volume mapped cube by cube to the same CME time, but using a different reconstructed volume, allows the measurement of these same features element by element in the other parameter space. The highlighted density volume can then be applied to the 3D reconstructed velocity (v) volume, and for each cube within the volume the mass multiplied by $1/2\,v^2$ yields a kinetic energy associated with the outward flow of the CME material. Conversely, in the case of a velocity-defined 3D structure, the velocity volume can be mapped cube by cube to the density volume to determine a kinetic energy defined by the high velocity CME structure. Both of these methods of measuring CME extents and mapping their structure are demonstrated in figure 3. For this CME, the fast shock measured *in situ* by ACE was followed by a high speed cap of material, and finally, the associated dense structure. There is not much IPS velocity data available to the south of the Earth, so here the reconstructed velocity or *g*-level structure in the southern hemisphere is treated with caution. However, there are many observations to the north for this CME, and the velocities there do not show as high a speed over the solar north pole as it does in the ecliptic. Thus, although a

cap of high speed material generally precedes this CME, it is unlikely that this high speed is as extensive to the north as it is near the ecliptic and both to the west and east of the structure, which here appears as a dense loop from the north to the south of the solar equator.

Figure 4 again depicts this 3D reconstructed CME both in density, as in some portions of figures 2 and 3, and also as in brightness observed from Earth as in figure 1d. Superimposed on this reconstruction (figure 4b) is the 3D reconstructed flux rope cylinder measured in ACE *in situ* data (from [13]). Other studies have depicted these same magnetic features in conjunction with the CME loop-like dense structure [9, 10], but here we show the depicted structure superimposed and displayed relative to all the other portions of the CME. It is undeniable that the flux-rope cylinder in these magnetic reconstructions is oriented at Earth like the dense 3D reconstructed heliospheric material. However, the dense material does not fill the flux rope cylinder, but is present only at its trailing edge near the Earth.
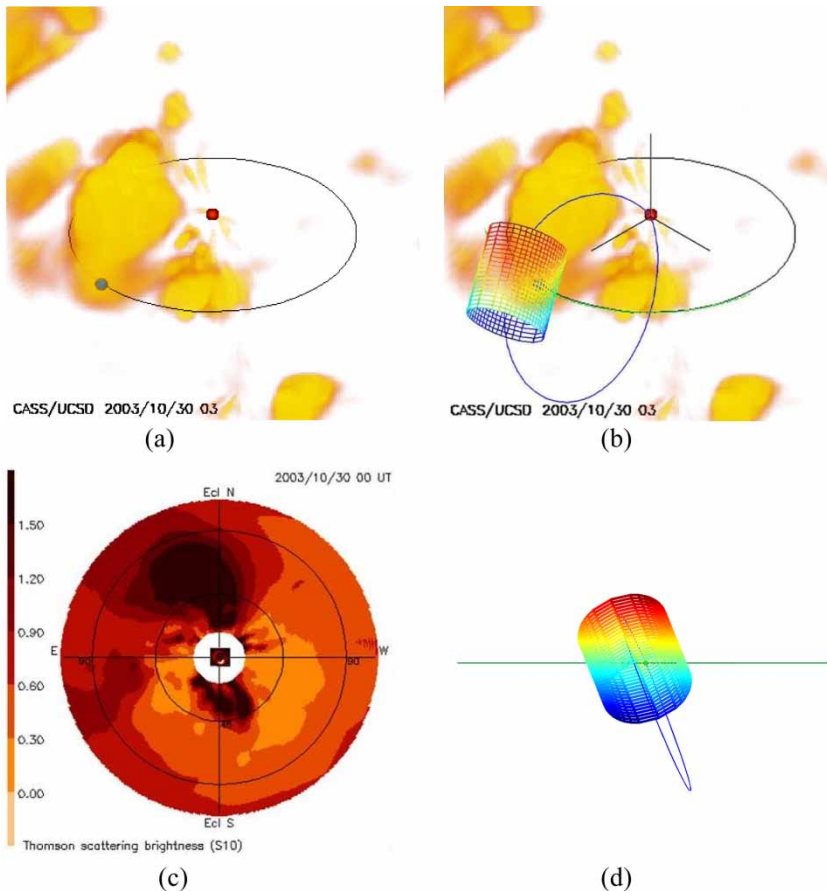

Figure 4. (a) 3D density reconstruction of the heliospheric response to the 28 October 2003 CME viewed from 3 AU 30° above the ecliptic plane and 45° West of the Sun–Earth line at a time intermediate to those of figures 2a and 2c. Earth is shown as a blue circle in its orbit, Sun by a red circle in the centre. Contours are from $10\,e^-\,cm^{-3}$ to $30\,e^-\,cm^{-3}$ and have an r^{-2} density gradient removed. A portion of the ejecta associated with a solar prominence is here observed to the south of the Sun (from [7]). (b) Same as (a), but with the reconstructed flux rope cylinder from ACE superposed. (c) 2D heliospheric sky map as seen from Earth in Thomson-scattering brightness. An 11:06 UT image of the CME from the LASCO C2 coronagraph is superposed (centre) at its appropriate size. (d) The flux rope cylinder viewed from behind the Earth looking directly toward the Sun without perspective. The horizontal line marks the ecliptic and has a length of 2 AU (from [13]).

4. Results

Table 1 summarizes the mass and energy determinations for the various UCSD 3D reconstructions shown in figures 2d, 3a, and 3c, for the 28 October 2003 CME. Column one of table 1 gives the item measured, column 2 gives the volume enclosed by the contour, column 3 shows its excess mass assuming each electron is associated with 2×10^{-24}g of material (assuming a 10% helium abundance), and column 4 gives the energy for the structure measured derived from the total mass and IPS reconstructed velocities. These mass and energy values are relatively large compared to some other CMEs that we have measured, and can be compared with LASCO CME mass determinations for the same event. The northernmost CME structure in LASCO C3 data provides an excess mass of 0.5×10^{16}g assuming the CME is in the plane of the sky. Instead, if the average distance were to be at 60° from the plane of the sky, the excess mass for this portion of the event would become $\sim 1.5 \times 10^{16}$g (Vourlidas, private communication, 2004). This same material has an excess mass of 3.2×10^{16}g in the IPS 3D reconstruction, and an excess mass of 6.7×10^{16}g in the SMEI 3D reconstructions (from [7]). The total excess mass of this whole CME inner structure to the north and south of the equator is 11.4×10^{16}g measured from the SMEI-reconstructed volumes. In LASCO C3 observations, the CME mass to the south of the ecliptic is 1.4×10^{16}g if the material is completely contained in the plane of the sky; and if 40° from the plane of the sky, it has an excess mass of 1.8×10^{16}g (Vourlidas, private communication, 2004). These values compare with $(11.4 - 6.7) \times 10^{16}$g $= 4.7 \times 10^{16}$g of material in the southern hemisphere measured in the SMEI 3D reconstructions. Thus, the SMEI reconstructed data show perhaps a factor of two to three more mass than the LASCO C3 observations in these preliminary data analyses. Given the approximations in determining both LASCO and the reconstructed 3D values, this is a good match, but the difference is of interest since both the IPS and the SMEI analyses show somewhat higher masses than the LASCO C3 observations, and this difference is probably outside of the expected measurement error. Thus, it is likely that a portion of the excess mass measured in the SMEI and IPS observations is either derived from the ambient solar wind, or from material outside of the coronagraph field of view.

The average outward motion of the dense material measured in the IPS and SMEI 3D reconstructions is $\sim$800 km s^{-1}, far slower that the initial shock transit time of 19 hours (an average of $\sim$2000 km s^{-1}) [14]; or the speed of the solar wind reconstructed in the high-speed cap of material in front of the ejected mass. The speeds measured *in situ* at ACE for this material reach values of up to 1800 km s^{-1} [15], and are reconstructed using IPS velocity measurements to values > 1500 km s^{-1} in some portions of the leading cap of high-speed material. The mass contained within the high speed solar wind cap above the 900 km s^{-1} 3D contour exceeds 1.0×10^{16}g.

The kinetic energies here (table 1, final column) are determined volume-element by volume-element, from one 3D reconstructed volume to the other. Given the 28 October 2003 CME is

Table 1.   28 October 2003 CME volume, mass, and energy.

Item	Volume (AU^3)	Mass ($\times 10^{16}$g)	Energy ($\times 10^{32}$ ergs)
Northern CME structure (IPS – figure 2d)	0.18	3.2 (excess) 4.5 (total)	1.8
Total CME dense structure (SMEI – figure 3a)	0.41	11.4 (excess) 14.2 (total)	4.5
High velocity region (IPS – figure 3c)	0.30	1.0 (excess) 1.8 (total)	0.8

much faster than the ambient wind, it is pretty certain that the higher speed is indicative of an initial energy input responsible for the CME, and that many of the strong forces at CME initiation are still represented by this outward fast-moving material. Even so, measurement of the CME energy at this late stage of the event has not been fully explored using the SMEI and IPS analyses, and in general especially for slower events these energies may simply be indicative of the general outward solar wind flow. For the 28 October 2003 CME the energy measured is undoubtedly mostly from the CME and very little from a blend with the background solar wind.

In figure 4b, the magnetic field loop structure is entrained in the outward flow of the plasma, and must primarily conform to the plasma outward motion. As long as the location of the dense structure follows the magnetic field lines, the loop (shown schematically) now has its approximate location determined better than would result by simply using an extrapolation from the *in situ* measurements near Earth. This implies that the loop continues to the north somewhat more than in the schematic, and must bend sharply sunward to the south more to include the slower-velocity material moving outward to the south of the Sun. In coronagraph observations, a loop-like CME is often observed with a three-part structure; a bright outer portion, a darker void region, and a bright inner core. In the present case, it is fairly certain that the void region is represented by this magnetic flux rope cylinder, while the dense material forming the north–south loop is the bright central inner CME core. Here, the size of the heliospheric structure implied associated with the CME is enormous and encompasses most of the earthward-facing hemisphere.

5.   Remotely-sensed heliospheric magnetic fields

In figure 4, a magnetic field flux cylinder reconstructed from *in situ* spacecraft measurements is depicted, and in previous studies [16] we show a way to extrapolate magnetic fields from the solar surface. However, until it is possible to remotely view heliospheric magnetic fields, the actual shapes of these structures and how they interact and are associated with the dense and high velocity structures will remain the province of multi-spacecraft observations. Faraday Rotation (FR), the changing polarization plane of an electromagnetic wave as it propagates through a magnetized medium, can probe the coronal and heliospheric magnetic field. The magnetized plasma of the solar atmosphere is a birefringent medium through which left- and right-circularly polarized components of the electromagnetic wave travel at different speeds. If the magnetic field is parallel to the direction of propagation of the wave, the phase velocity of the right-circularly polarized component is faster than that of the left. This rotates the plane of polarization in a right-handed sense along the direction of propagation.

Extracting the magnetic field from FR measurements is a geometrically detailed problem. The rotation angle ϕ is the integral of the electron density times the magnetic field component parallel to the line of sight:

$$\phi \propto \lambda^2 \int n_e \, \vec{B} \bullet \vec{dS} \tag{1}$$

where λ is the wavelength, n_e is the electron density along the line-of-sight interval dS, and B is the magnetic field vector. 3D electron densities are obtained using tomographic techniques from IPS and SMEI data.

Magnetic field measurements of the solar corona using FR are currently infrequent and limited to a few radio sources [17, 18]. However, antennas and receivers suitable for measuring the FR of the solar corona from natural radio sources presently exist (the VLA; see [19, 20]; and at Effelsberg, see [21]; or Arecibo, see [22]) or are currently under development [23] in

the Netherlands (LoFAR) and Australia (MWA). The new systems may allow a determination of coronal FR within as close as 60 R_s of the Sun (at 240 MHz), and possibly to elongations of 60° or more (at 60–80 MHz). The frequency of the probing signal must be above the maximum plasma frequency along the line of sight; this limitation sets the inner boundary of FR measurements. The outer boundary is set by the amount of rotation exceeding the measurement error from the receiving system's sensitivity.

As a parcel of coronal plasma moves away from the Sun, line-of-sight observations through the plasma measure different amounts of FR. When such FR data are available, decoding and analysing these, employing techniques similar to those used for the 3D reconstructions of heliospheric density and velocity, may become as commonplace for getting vector magnetic fields as they are for these other 3D reconstructions. Interpreting these observations in terms of vector magnetic fields and their interactions with objects imbedded in the plasma (planets, comets, and interplanetary spacecraft) could potentially truly revolutionize heliospheric physics.

6. Summary

We have developed a tomographic technique that employs heliospheric remote-sensing data obtained from a single observing location, and reconstructs the density and velocity distribution of CMEs. This enables studying CMEs as they propagate through the inner heliosphere to the Earth. We have applied this tomographic technique to heliospheric observations, currently available as observations from STELab in Japan, and as data taken from SMEI. The analyses show several important features and give an accounting of the mass and energy of the CME structure as it moves outward into the heliosphere. Combined with magnetic field observations from the ACE spacecraft, and the *in situ* magnetic field reconstructions near Earth, these observations show one of the best examples of the many components of a heliospheric CME and its extrapolation from coronal distances to near Earth. In the case of the 28 October 2003 CME, this is manifest as a huge, energetic event that encompasses nearly a hemisphere of the Sun in the earthward direction, and shows at least a portion of CME three-part coronal structure present at the distances of Earth. Only when remote-sensing heliospheric observations of magnetic fields are available will the true extent and global aspect of CMEs and their interactions with interplanetary bodies be known and understood.

Acknowledgements

References

[1] A. Hewish, P.F. Scott, D. Wills, Interplanetary scintillation of small diameter radio sources. Nature **203** 121 (1964).
[2] Z. Houminer. Corotating plasma streams revealed by interplanetary scintillation. Nature Phys. Sci. **231** 165 (1971).
[3] M. Kojima, T. Kakinuma. Solar-cycle evolution of solar wind speed structure between 1973 and 1985 observed with the interplanetary scintillation method. J. Geophys. Res. **92** 7269 (1987).
[4] B.V. Jackson, A. Buffington, P.P Hick *et al.*, The Solar Mass Ejection Imager (SMEI) Mission. Solar Phys. **225** 177 (2005).

[5] B.V. Jackson, P.L. Hick, M. Kojima *et al.*, Heliospheric Tomography Using Interplanetary Scintillation Observations 1. Combined Nagoya and Cambridge data. J. Geophys. Res. **103** 12,049 (1998).

[6] B.V. Jackson, P.P. Hick, Three-dimensional tomography of interplanetary disturbances. In *Solar and Space Weather Radiophysics, Current Status and Future Developments*, Astrophysics and Space Science Library, **314**, D.E. Gary and C.U. Keller (Eds.), Chapter 17, pp. 355–386, Kluwer Academic Publishers, Dordrecht, The Netherlands (2005).

[7] B.V. Jackson, A. Buffington, P.P. Hick *et al.*, Preliminary three-dimensional analysis of the heliospheric response to the 28 October 2003 CME using SMEI white-light observations. J. Geophys. Res. **111** A4, A04S91 (2006).

[8] B.V. Jackson, J.A. Boyer, P.P. Hick *et al.*, Analysis of solar wind events using interplanetary scintillation (IPS) remote sensing 3D reconstructions and their comparison at Mars. Solar Phys. **241** 385 (2007).

[9] M. Tokumaru, M. Kojima, K. Fujiki *et al.*, Toroidal-shaped interplanetary disturbance associated with the halo coronal mass ejection event on 14 July, 2000. J. Geophys. Res. **108 (A5)** 1220, doi:10.1029/2002ja009574 (2003).

[10] M. Tokumaru, M. Kojima, K. Fujiki *et al.*, The source and propagation of the interplanetary disturbance associated with the full-halo coronal mass ejection on 2003 October 28. J. Geophys. Res., **112**, A05106, doi: 10.1029/2006JA012043 (2007).

[11] G.E. Brueckner, R.A. Howard, M.J. Koomen *et al.*, The Large Angle Spectroscopic Coronagraph (LASCO): visible light coronal imaging and spectroscopy. Solar Phys. **162** 357 (1995).

[12] B.V. Jackson, P.P. Hick, A. Buffington *et al.*, Time-dependent tomography of heliospheric features using interplanetary scintillation (IPS) remote-sensing observations. Solar Wind 10 Conference Proceedings, Pisa, June 17–21, 31 (2002).

[13] E.A. Jensen, T. Mulligan, B.V. Jackson *et al.*, 3-D Magnetic Field Geometry of the October 28, 2003 ICME: Comparison with SMEI White-Light Observations. EOS Trans. AGU **87(52)**, Fall Meet. Suppl., Abstract SH33A-0397 (2006).

[14] E.W. Cliver, L. Svalgaard, The 1859 solar-terrestrial disturbance and the current limits of extreme space weather activity. Solar Phys. **224** 407 (2004).

[15] R.M. Skoug, J.T. Gosling, J.T. Steinberg *et al.*, Extremely high speed solar wind: 29–30 October 2003. J. Geophys. Res. **109** A09102, doi:10.1029/2004JA010494 (2004).

[16] T. Dunn, B.V. Jackson, P.P. Hick *et al.*, Comparative Analyses of the CSSS Calculation in the UCSD Tomographic Solar Observations. Solar Phys. **227** 339 (2005).

[17] M.K. Bird, P. Edenhofer, Remote sensing observations of the solar corona. In *Physics of the Inner Heliosphere I*, R. Schwenn and E. Marsch, (eds.), pp. 13–97, Springer-Verlag, Berlin (1990).

[18] E.A. Jensen, M.K Bird, M. Paetzold *et al.*, The Cassini Solar Conjunction Faraday Rotation Experiment. Adv. Space Res. **36** 1587 (2005).

[19] S. Mancuso, S.R. Spangler, Coronal Faraday rotation observations: measurements and limits on plasma inhomogeneities. Astrophys. J. **525** 195 (1999).

[20] S. Mancuso, S.R. Spangler, Faraday rotation and models for the plasma structure of the solar corona. Astrophys. J. **539** 480 (2000).

[21] M.K. Bird, E. Schrufer, H. Volland *et al.*, Coronal Faraday rotation during solar occultation of PSR 0525+21. Nature **283** 459 (1980).

[22] M.K. Bird, H. Volland, R.A. Howard *et al.*, White-light and radio sounding observations of coronal transients. Solar Phys. **98** 341 (1985).

[23] J.E. Salah, C.J. Lonsdale, D. Oberoi *et al.*, Space weather capabilities of low frequency radio arrays. Proc. SPIE **5901** 59010G-1 (2005).